

Cite this article as: Du Licheng, Gao Feng, Dong Zhuolin. Mechanical Behavior and Constitutive Equation of High Temperature Compression Deformation of IN706 Superalloy[J]. Rare Metal Materials and Engineering, 2024, 53(08): 2182-2192. DOI: 10.12442/j.issn.1002-185X.E20230045.

ARTICLE

# Mechanical Behavior and Constitutive Equation of High Temperature Compression Deformation of IN706 Superalloy

Du Licheng, Gao Feng, Dong Zhuolin

AECC Aero Science and Technology Co., Ltd, Chengdu 610503, China

**Abstract:** IN706 superalloy is particularly sensitive to the parameters of hot working process. The flow stress of the IN706 superalloy was investigated during reduction deformation of 30%, 45%, and 60% under the isothermal compression conditions of temperature at 1143–1393 K and strain rate at 0.01, 0.1, 0.5, and 1 s<sup>-1</sup>. The exponent-type Zener-Hollomon equation was used to describe the impact of strain and temperature on the thermal deformation. Meanwhile, the strain effect of various material constants, such as  $\alpha$ ,  $n$ ,  $Q$ , and  $\ln A$ , was considered in the constitutive equation considering the strain compensation, and the correlation coefficient  $R$  and the average absolute relative error were verified. On the basis of constitutive equation construction, the hot processing map of IN706 superalloy was drawn, and the instability region was obtained based on the Murty criterion. Results show that the reasonable thermal working process parameter window is strain rate of 0.1 s<sup>-1</sup> and temperature of 1313–1353 K.

**Key words:** IN706 superalloy; mechanical behavior; constitutive equation; hot processing map; strain effect

Turbine disc is one of the core hot end components in gas turbines. As the carrier of turbine rotor blades, turbine disc bears the rotation load of hot end during operation, and its forming quality is important to the whole gas turbine. Based on the chemical content modification of Mo, Nb, and Ti elements, precipitation strengthening with reduced segregation occurs in IN706 superalloy, which is caused by coherent Ni<sub>3</sub>X-type compounds, such as Ni<sub>3</sub>Nb and Ni<sub>3</sub>(Al, Ti)<sup>[1-3]</sup>. IN706 superalloys gradually replace steel parts in gas turbines due to their high mechanical strength, fine formability, and good machinability. Coherent  $\gamma'$  (Ni<sub>3</sub>Al) and  $\gamma''$  (Ni<sub>3</sub>Nb) intermetallic phases formed by aging heat treatment are the primary factors to enhance the resistance and strength of IN706 superalloy<sup>[4]</sup>. Therefore, IN706 superalloy has been applied to manufacture large structural parts, including turbine disks, shafts, motor mounts, and diffuser cases in power generation and aero-space industries<sup>[5-7]</sup>.

The hot working preparation for superalloys is usually ameliorated based on the hot compression test results. Moreover, IN706 superalloy is particularly sensitive to the parameters of hot working process. Generally, the microstructure of Inconel alloys consists of  $\gamma'$ ,  $\gamma''$ ,  $\eta$  (Ni<sub>3</sub>Ti),

(Nb, Ti, Ni)C carbides, and Laves phases in the face-centered cubic (fcc)  $\gamma$  matrix<sup>[8]</sup>. In the process of plastic deformation, the evolution of precipitated phase inside the material is as follows. Firstly,  $\gamma'/\gamma''$  coprecipitates are coherent with the  $\gamma$  matrix, and additional energy is required for further deformation<sup>[9-11]</sup>. Secondly, if the precipitation size exceeds 25 nm, precipitation coherency loss may be induced in the matrix, resulting in the weakening of the precipitation hardening effect<sup>[12]</sup>. Meanwhile, the sizes of carbides and  $\eta$  phase in Inconel alloys are larger than that of  $\gamma'/\gamma''$  co-precipitates, and  $\eta$  phase reduces the strength during plastic deformation<sup>[13]</sup>. In addition to the change in geometric shape, the microstructure of IN706 superalloy also produces complex changes during the deformation process at high temperature. Deformation temperature, strain rate, and deformation degree are the main factors affecting the deformation behavior of metal materials at high temperature. The establishment of plastic deformation constitutive equation related to the abovementioned factors is the premise of process design and numerical simulation of plastic deformation process of metal materials, which is very important for the practical engineering problems, such as the rational formulation of forging process, the control of forging

Received date: October 19, 2023

Corresponding author: Du Licheng, Ph. D., AECC Aero Science and Technology Co., Ltd, Chengdu 610503, P. R. China, E-mail: 115418225@qq.com

Copyright © 2024, Northwest Institute for Nonferrous Metal Research. Published by Science Press. All rights reserved.

structure and properties, and the selection of forging equipment.

IN706 superalloy is generally used after precipitation hardening, and the hardening treatment is commonly two-step aging or direct aging, which can achieve optimum tensile strength. Besides, the three-step aging with h-stabilization treatment can achieve better creep/rupture properties<sup>[14-15]</sup>. Kim et al<sup>[16]</sup> studied the effect of post-heat treatment on the deformation mechanisms of IN706 superalloy and found that the heat treatment conditions could affect the morphology of precipitates in the matrix, resulting in different deformation behavior. Marsh et al<sup>[17]</sup> mentioned that  $\gamma'$  phase content affected the dynamic strain aging effect and increased the stress amplitude during plastic deformation. Kim et al<sup>[18]</sup> investigated the effects of the stabilization conditions on the microstructure evolution in Ni-Fe-based IN706 superalloy and the relationship between the microstructure and tensile and creep properties. Wanderka et al<sup>[19]</sup> characterized  $\gamma'$  and  $\gamma''$  precipitates with sizes of 15–20 nm in stabilized Inconel 706 alloy, and the atom probed tomography results indicated that the disc-shaped  $\gamma''$  phase was larger than the spherical  $\gamma'$  phase, and it was rich in Nb and Ti with a small amount of Al. Shibata et al<sup>[20]</sup> reported that the precipitation of the  $\eta$  phase at the grain boundaries effectively inhibited the grain boundary sliding. However, the microstructural investigation of the blocking effect of the  $\eta$  phase at the grain boundaries is insufficient.

As the foundation of engineering part production, thermal deformation processes require not only the information of alloy microstructure and mechanical properties but also the dimensional accuracy<sup>[21]</sup>. The constitutive equation can reflect the flow behavior of the plastic deformation of the material, reveal the physical mechanism of the plastic deformation, and provide a reference for the finite element numerical simulation. The influence of strain is proven to be necessary for the verification of constitutive equation involving the strain effect, which predicts flow behavior of pure titanium<sup>[22]</sup>, titanium alloys<sup>[23]</sup>, steel<sup>[24-26]</sup>, and aluminum alloys<sup>[27-28]</sup> at elevated temperatures. The higher the accuracy of the constitutive equation, the less the difference in the simulated and experimental plastic deformation results. Thermal working diagram is a process graph formed by superposition of energy dissipation rate curves and plastic deformation instability curves based on dynamic material model, which can describe the dynamic response of materials to thermal deformation parameters and reflect the internal microstructure change mechanism during material deformation. The machinability of IN706 superalloy can be evaluated by thermal working diagram, which can provide reference for the study of strength and toughness mechanism of IN706 superalloy.

Therefore, the thermal deformation behavior of IN706 superalloy was studied in this research based on the simulated thermal compression tests. Firstly, the simulated orthogonal

thermal compression tests were conducted. Then, the high temperature constitutive equation based on Arrhenius model considering strain compensation was established. Finally, the hot working diagram of IN706 superalloy with the experiment parameter ranges was established, and the hot working process parameter window could be optimized.

## 1 Experiment

The experiment material was IN706 superalloy, and its strengthening phase mainly consists of  $\gamma'$  and  $\gamma''$  phases. The main composition of IN706 superalloy is shown in Table 1.

The test specimen was cylindrical and finished with  $\Phi 10$  mm $\times$ 15 mm in dimension. The simulated orthogonal thermal compression test was conducted by Gleeble-3500 tester (DSI Corporation, New York, USA) with parameter setting. The Gleeble-3500 thermal/force simulation testing machine adopts computer programming control, which can accurately measure the test parameters, such as temperature, strain rate, stress, and strain, and collect test data through computer in real time. The upper and lower end faces were parallel to each other. The mechanical perpendicularity of the vertical face was maintained, and the two end surfaces were smooth to decrease the effects of transverse friction on deformation. The axis of the cylindrical specimen was the axial line of the bar billet. In the experiment, a radial sensor was used in the deformation of the specimen to measure the cross-section area and the collected signals were used to control the tester parameters. The specimen was compressed under a constant strain rate, and the temperature deviation was controlled as  $\pm 1$  K. During the test, the loading chamber was vacuumed to prevent oxidation at high temperature, and the specimen was quenched by water cooling system.

The temperature of simulated isothermal compression experiment was 1143, 1193, 1243, 1273, 1283, 1293, 1313, 1353, and 1393 K. The strain rate was 0.01, 0.1, 0.5, and 1 s<sup>-1</sup>, and the reduction amount was 30%, 45%, and 60%, as shown in Fig. 1. A graphite flake cushion was used between the specimen and the pressure head to decrease transverse friction. The specimen was heated to deformation temperature at heating rate of 10 K/s, and it was maintained at designed temperature for 3 min for temperature uniformity. Thermal deformation occurred under the isothermal constant strain rate. The stress-strain curves were automatically recorded during the isothermal compression at elevated temperatures.

## 2 Result and Discussion

### 2.1 Experiment results and flow stress behavior

According to the test scheme of IN706 superalloy, 108 thermal simulated compression specimens were tested under different temperature, strain rate, and reduction deformation conditions. After hot deformation, water cooling was used to

Table 1 Chemical composition of IN706 superalloy (wt%)

C	Mn	Si	P	S	Ni	Cr	Ti	Al	B	Cu	Nb	Ta	Fe
0.06	0.35	0.35	0.02	0.015	39–44	14.5–17.5	1.5–2.0	0.4	0.006	0.3	2.5–3.3	0.05	Bal.

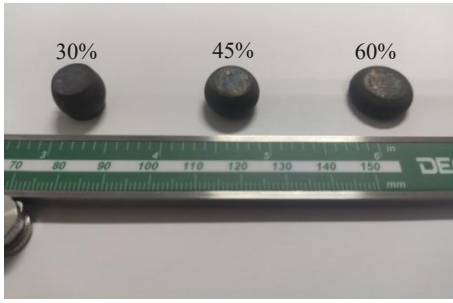


Fig.1 Appearance of IN706 specimens after different reduction deformation

retain the microstructure under high temperature deformation conditions. The Gleeble-3500 thermal/force simulation testing machine was used to conduct thermal compression tests, and the stress-strain curves of the specimens under different conditions are shown in Fig.2.

It can be seen that under the same strain rate, the flow stress of IN706 superalloy specimens is decreased with the increase in deformation temperature. This is because with the increase in deformation temperature, the thermal activation effect of the material is enhanced, the average kinetic energy of metal atoms is increased, and the amplitude of atomic vibration is increased, resulting in the increase in dislocation and vacancy activity and the enhancement of slip system. Thus, the plasticity of IN706 superalloy is enhanced and the deformation resistance degrades. During the high temperature deformation, dynamic recovery and dynamic recrystallization are the main softening mechanisms of plastic deformation of metal materials.

Correspondingly, under the same deformation temperature condition, the stress of IN706 superalloy is increased with the

increase in strain rate. This is because the deformation storage energy of metal materials is increased with the increase in strain rate, and the plastic deformation cannot be fully completed in the deformation body, resulting in more elastic deformation and more obvious work hardening effect. Therefore, the deformation resistance of the IN706 superalloy increases.

The shape characteristics of the stress-strain curves are useful to determine the hot deformation mechanism of IN706 superalloy, which mainly depends on the strain rate and deformation temperature during the hot deformation process. As shown in Fig. 2, when the deformation temperature is greater than 1243 K, the stress-strain curves mainly present the steady dynamic recovery flow feature. Therefore, dynamic recovery is the main softening mechanism under these thermal deformation conditions, which can be identified through the dislocation climbing and cross-slip.

## 2.2 Constitutive modeling

### 2.2.1 Constitutive equation derivation

The influence of temperature and strain rate on the thermal deformation behavior of materials can be characterized by Zener-Hollomon parameter  $Z$ , and the specific influence law obeys the exponential relationship, as follows:

$$Z = \dot{\epsilon} \exp(Q/RT) \quad (1)$$

where  $Q$  is the deformation activation energy ( $\text{J}\cdot\text{mol}^{-1}$ );  $R$  is the universal gas constant ( $R=8.314 \text{ J}\cdot\text{mol}^{-1}\cdot\text{K}^{-1}$ );  $\dot{\epsilon}$  is strain rate ( $\text{s}^{-1}$ );  $T$  is the deformation temperature (K).

The Arrhenius model is a widely used constitutive model in phenomenological constitutive equations, which can describe the deformation process of materials, especially the relationship among flow stress, strain rate, and deformation temperature under high temperature deformation conditions. It is generally believed that the deformation process of materials

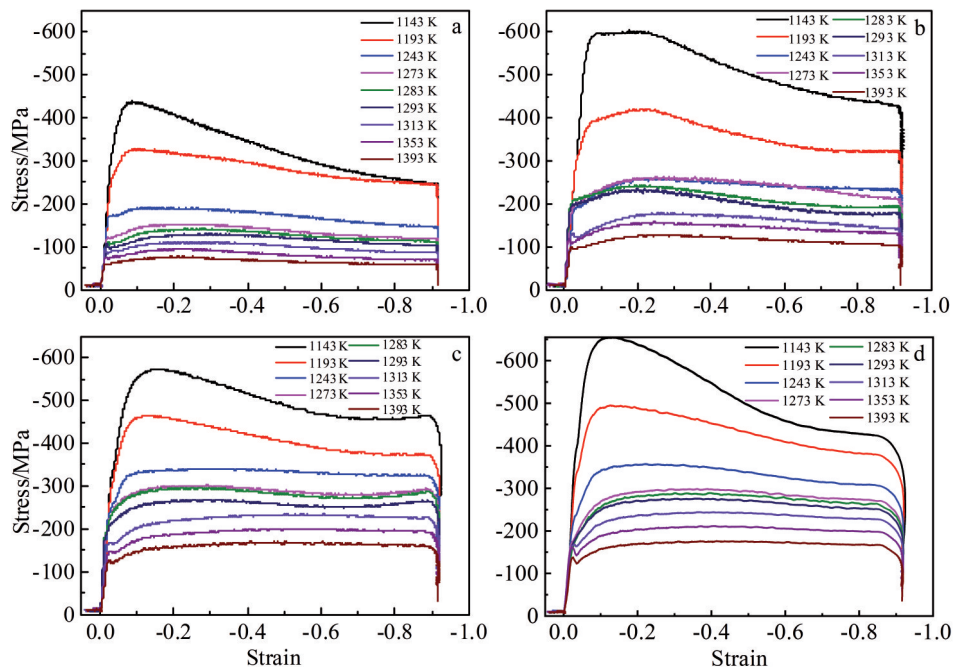


Fig.2 Stress-strain curves of IN706 superalloy at different temperatures and strain rates: (a)  $0.01 \text{ s}^{-1}$ , (b)  $0.1 \text{ s}^{-1}$ , (c)  $0.5 \text{ s}^{-1}$ , and (d)  $1 \text{ s}^{-1}$

under high temperature conditions is a thermal activation process, which is related to the strain rate, strain, and deformation temperature. Besides, the deformation rate is controlled by the thermal activation process and follows the Arrhenius equation law, as follows:

$$\dot{\epsilon} = AF(\sigma)\exp(-Q/RT) \tag{2}$$

where  $F(\sigma)$  is a function of stress and  $A$  is material constant.  $F(\sigma)$  has three expressions, as follows:

$$F(\sigma) = \sigma^{n'} \quad \alpha\sigma < 0.8 \tag{3}$$

$$F(\sigma) = \exp(\beta\sigma) \quad \alpha\sigma > 1.2 \tag{4}$$

$$F(\sigma) = [\sinh(\alpha\sigma)]^n \quad \text{For all } \sigma \tag{5}$$

where  $n'$ ,  $\beta$ ,  $\alpha$ , and  $n$  are material constants. Additionally, the relationship among  $n'$ ,  $\beta$ , and  $\alpha$  is expressed in Eq. (6), as follows:

$$\alpha = \beta/n' \tag{6}$$

The power function Eq. (3) is applicable to the thermal deformation process with low stress; the exponential function Eq. (4) is applicable to the thermal deformation process with high stress; the hyperbolic sine function Eq.(5) is applicable to the thermal deformation process with a wide stress range.

### 2.2.2 Material constants

The Zener-Hollomon parameter  $Z$  (temperature-compensated strain rate factor) in Eq. (1) can be used to characterize the relationship between strain rate and deformation temperature. According to Eq.(2) and Eq.(5), the primary task of the Arrhenius model establishment is to determine  $Q$ ,  $\alpha$ ,  $n$ ,  $\ln A$ , and other material constants. After determining these material constants, the material flow stress under deformation conditions can be calculated according to Eq.(5). In this research, the determination process of material parameters is conducted with strain  $\epsilon=0.2$ .

By solving Eq.(2-4), Eq.(7-8) can be obtained, as follows:

$$\dot{\epsilon} = B\sigma^{n'} \quad \text{For } \alpha\sigma < 0.8 \tag{7}$$

$$\dot{\epsilon} = C \exp(\beta\sigma) \quad \text{For } \alpha\sigma > 1.2 \tag{8}$$

where  $B$  and  $C$  are material parameters.

Taking natural logarithm of both sides of Eq. (7 – 8), Eq.(9-10) can be obtained, respectively, as follows:

$$\ln \sigma = \frac{1}{n'} \ln \dot{\epsilon} - \frac{1}{n'} \ln B \tag{9}$$

$$\sigma = \frac{1}{\beta} \ln \dot{\epsilon} - \frac{1}{\beta} \ln C \tag{10}$$

The stress and strain rate obtained from the tests under the condition of strain  $\epsilon=0.2$  are substituted into Eq.(9-10), and the  $\ln\sigma$ - $\ln\dot{\epsilon}$  and  $\sigma$ - $\ln\dot{\epsilon}$  curves are shown in Fig. 3a and 3b, respectively. The data points are linearly fitted. It can be seen that the fitting lines under different temperature conditions are almost parallel to each other. The parameters  $n'$  and  $\beta$  can be obtained from the slopes of the curves. In this research, through linear fitting, the slope of fitting line and average result value are obtained. Then, the average values of parameters  $n'$  and  $\beta$  under different temperature conditions are obtained. After calculation, the  $n'$  and  $\beta$  parameters are 7.3109 and 0.0329, respectively, and  $\alpha=\beta/n'=0.0045$ .

Considering all stress-strain conditions, Eq. (2) can be expressed as follows:

$$\dot{\epsilon} = A[\sinh(\alpha\sigma)]^n \exp(-Q/RT) \tag{11}$$

Taking natural logarithm of the both sides of Eq. (11), Eq.(12) is obtained, as follows:

$$\ln[\sinh(\alpha\sigma)] = \frac{\ln \dot{\epsilon}}{n} + \frac{Q}{nRT} - \frac{\ln A}{n} \tag{12}$$

Under certain temperature conditions, Eq. (12) can be expressed as Eq.(13), as follows:

$$\frac{1}{n} = \frac{d\{\ln[\sinh(\alpha\sigma)]\}}{d(\ln \dot{\epsilon})} \tag{13}$$

Therefore, the value of parameter  $n$  can be calculated from the slope of the  $\ln[\sinh(\alpha\sigma)]$ - $\ln\dot{\epsilon}$  curve, as shown in Fig. 4. After calculation, under the condition of strain  $\epsilon=0.2$ , the value of parameter  $n=4.8388$ .

Eq.(12) can be further expressed as follows:

$$Q = Rn \frac{d\{\ln[\sinh(\alpha\sigma)]\}}{d(1/T)} \tag{14}$$

When the abscissa changes from  $1/T$  to  $1000/T$ , the unit of the corresponding ordinate  $Q$  changes from J/mol to kJ/mol, and the  $Q$  value can be obtained by the slope, as shown in Fig. 5. The average  $Q$  value obtained by calculation is 635.1949 kJ/mol. The deformation activation energy  $Q$  represents the energy required for the atomic transition, and it is the most important physical parameter to reflect the deformation resistance of the material, which is generally considered to be closely related to the climbing, dynamic recovery, and dynamic recrystallization of dislocations,

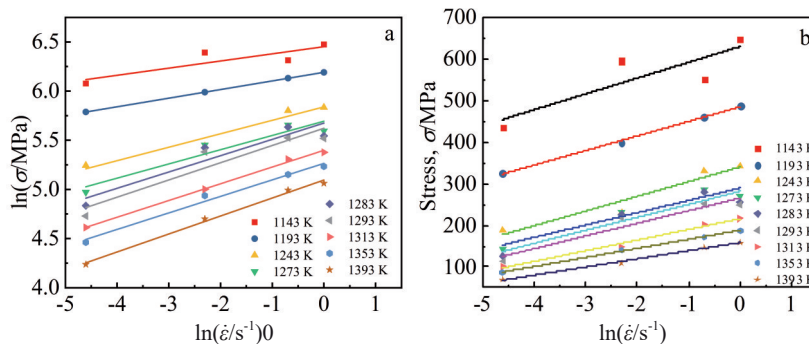


Fig.3 Relationships of  $\ln\sigma$ - $\ln\dot{\epsilon}$  (a) and  $\sigma$ - $\ln\dot{\epsilon}$  (b) under different temperature conditions

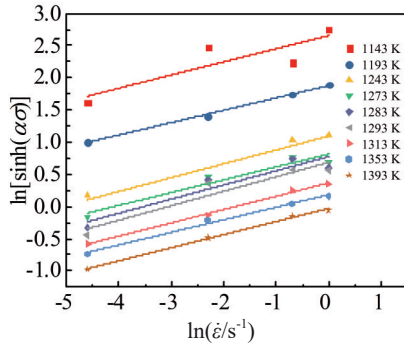


Fig.4 Relationship of  $\ln[\sinh(\alpha\sigma)] - \ln\dot{\epsilon}$  under different temperature conditions

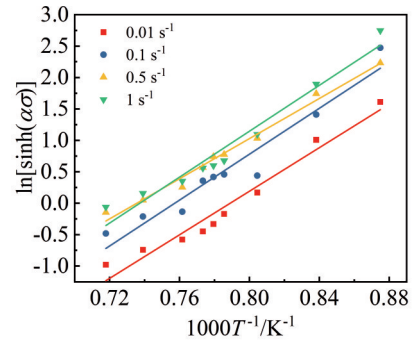


Fig.5 Relationship of  $\ln[\sinh(\alpha\sigma)] - 1000/T$  under different strain rate conditions

revealing the basic characteristics of plastic deformation of the materials.

After the  $Q$  value is obtained,  $\ln A$  can be calculated by the ordinate intercept of the linear fitting lines in Fig. 5, and the calculated value of parameter  $A$  is  $1.5064 \times 10^{24} \text{ s}^{-1}$ . In summary, the material parameters ( $\alpha$ ,  $n$ ,  $Q$ , and  $\ln A$ ) of the Arrhenius constitutive equation can be obtained, and similar processes can be used under other strain conditions.

### 2.2.3 Strain effect

It is well known that the strain of the material barely has influence on the flow stress during the high temperature deformation, and the abovementioned material parameters ( $\alpha$ ,  $n$ ,  $Q$ , and  $\ln A$ ) are generally considered as constants, i.e., they do not change with the strain. Thus, the strain term is ignored in Eq.(1). However, in recent years, more and more researches reported that the  $\alpha$ ,  $n$ ,  $Q$ , and  $\ln A$  in constitutive equations of metals, especially alloy materials, changed with the increase in strain and presented a certain regularity. Therefore, the  $\alpha$ ,  $n$ ,

$Q$ ,  $\ln A$ , and other material parameters should be considered as a function of the true strain  $\epsilon$ . In this research, the strain range of 0.1–0.8 with interval of 0.1 was selected to analyze the variation in material parameters of the Arrhenius constitutive equation for IN706 superalloy with the strain, and the results are shown in Fig.6. Through analysis, the quintic polynomial fitting results of material parameters can be obtained by Eq.(15), as follows:

$$\begin{cases} \alpha = C_0 + C_1\epsilon + C_2\epsilon^2 + C_3\epsilon^3 + C_4\epsilon^4 + C_5\epsilon^5 \\ n = D_0 + D_1\epsilon + D_2\epsilon^2 + D_3\epsilon^3 + D_4\epsilon^4 + D_5\epsilon^5 \\ Q = E_0 + E_1\epsilon + E_2\epsilon^2 + E_3\epsilon^3 + E_4\epsilon^4 + E_5\epsilon^5 \\ \ln A = F_0 + F_1\epsilon + F_2\epsilon^2 + F_3\epsilon^3 + F_4\epsilon^4 + F_5\epsilon^5 \end{cases} \quad (15)$$

where  $C_0 - C_5$ ,  $D_0 - D_5$ ,  $E_0 - E_5$ , and  $F_0 - F_5$  are fitting coefficients.

As shown in Fig.6a, in addition to the first data point, the material parameter  $\alpha$  tends to increase with the increase in strain. However, other parameters, such as  $n$ ,  $Q$ , and  $\ln A$ , are decreased with the increase in strain without considering the last data point. The variation law of each material parameter

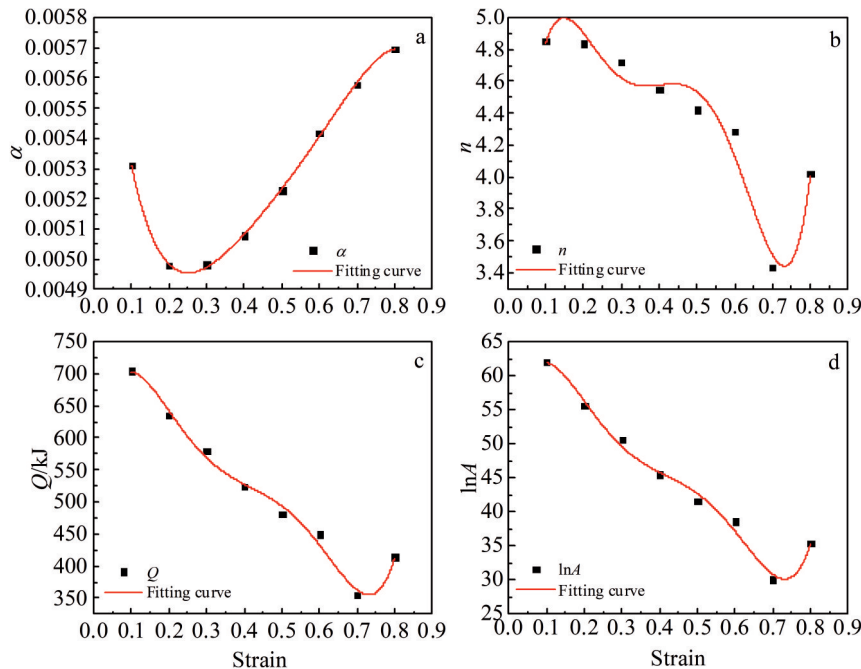


Fig.6 Relationships between strain and material parameters: (a)  $\alpha$ , (b)  $n$ , (c)  $Q$ , and (d)  $\ln A$

with strain  $\varepsilon$  can be accurately obtained by quintic polynomial, and the fitting accuracy, namely correlation coefficient  $R$ , is shown in Table 2.

**2.3 Verification of Arrhenius constitutive model**

By substituting Eq. (1) into Eq. (11), the Arrhenius constitutive equation of IN706 superalloy can be obtained, as expressed by Eq.(16), as follows :

$$\sigma = \frac{1}{\alpha} \ln \left\{ \left( \frac{Z}{A} \right)^{1/n} + \left[ \left( \frac{Z}{A} \right)^{2/n} + 1 \right]^{1/2} \right\} \quad (16)$$

The simulation results obtained from Arrhenius constitutive equation and the experiment results are shown in Fig. 7. It can be seen that the experimental and simulated stress values under different conditions are in good agreement, indicating that the established constitutive equation has good accuracy.

In order to quantify the simulation accuracy of the established constitutive equation, two statistical error quantification indexes are introduced: correlation coefficient  $R$  and average absolute value of relative error (AARE), as follows:

$$R = \frac{\sum_{i=1}^N (E_i - \bar{E})(P_i - \bar{P})}{\sqrt{\sum_{i=1}^N (E_i - \bar{E})^2 \sum_{i=1}^N (P_i - \bar{P})^2}} \quad (17)$$

$$AARE = \frac{1}{N} \sum_{i=1}^N \left| \frac{E_i - P_i}{E_i} \right| \times 100\% \quad (18)$$

where  $E_i$  is the experimental stress value (MPa);  $\bar{E}$  is the average experimental stress value (MPa);  $P_i$  is the simulated stress value (MPa);  $\bar{P}$  is the average simulated stress value (MPa);  $N$  is the total number of data.

$R$  is a commonly used statistical parameter, which represents the degree of linear correlation between the experimental and simulated data. The consistency between the experimental and simulated data cannot be accurately evaluated by the correlation coefficient. However, the absolute value of AARE is an unbiased statistical parameter as a representation of the relative error between data points. Therefore, AARE can be used to evaluate the accuracy of constitutive equation. The quantitative analysis results of the constitutive equation are shown in Fig.8. The calculated  $R$  is 0.9846 and AARE is 6.5922%, indicating that the constitutive equation of IN706 superalloy with strain compensation can

**Table 2 Values of polynomial fitting coefficients and correlation coefficients of material parameters**

Parameter	$\alpha$	$n$	$Q$	$\ln A$
Fitting coefficient	$C_0=0.006\ 33$	$D_0=2.411\ 03$	$E_0=574.868$	$F_0=50.746\ 22$
	$C_1=-0.015\ 39$	$D_1=47.863\ 68$	$E_1=3\ 255.273$	$F_1=288.509\ 2$
	$C_2=0.063\ 46$	$D_2=-314.177$	$E_2=-26\ 728.8$	$F_2=-2\ 391.03$
	$C_3=-0.122\ 69$	$D_3=894.797\ 3$	$E_3=79\ 652.47$	$F_3=7\ 139.159$
	$C_4=0.121\ 21$	$D_4=-1\ 156.21$	$E_4=-105\ 023$	$F_4=-9\ 422.34$
	$C_5=-0.048\ 12$	$D_5=548.783\ 8$	$E_5=50\ 583.28$	$F_5=4\ 541.279$
Correlation coefficient, $R$	0.999 34	0.964 04	0.992 9	0.993 16

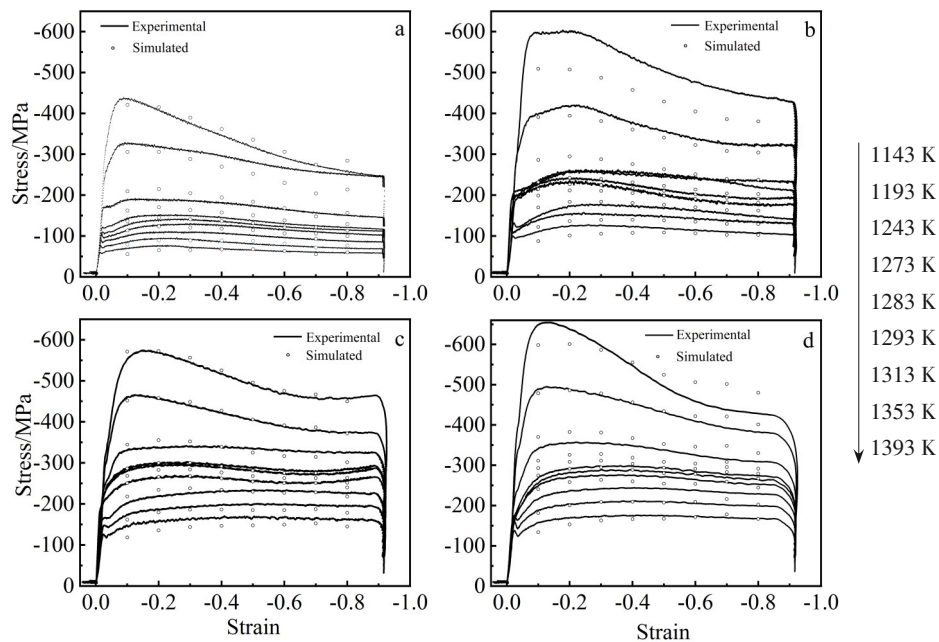


Fig.7 Experimental and simulated results at different stain rates: (a) 0.01 s<sup>-1</sup>, (b) 0.1 s<sup>-1</sup>, (c) 0.5 s<sup>-1</sup>, and (d) 1 s<sup>-1</sup>

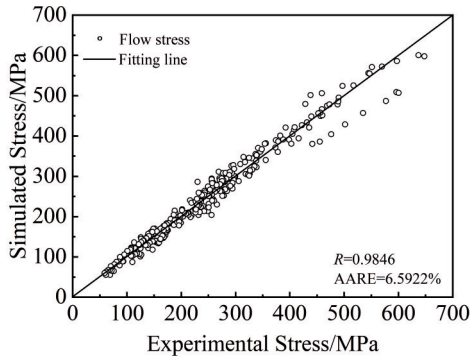


Fig.8 Correlation between simulated stress of constitutive equation and experimental stress

accurately describe the rheological behavior of the alloy under various thermal deformation conditions.

**2.4 Hot processing map**

As a process reference diagram based on dynamic material model, the hot processing map of materials is formed by superposition of energy dissipation rate curves and plastic deformation instability curves, reflecting the internal structure change mechanism of materials during deformation to a certain extent. The establishment of the hot processing map provides a basis for the feasibility analysis of the hot working process of materials, and the division of the safe zone and the unstable zone of plastic working provides a reference for the optimization of processing parameters.

In the hot processing map, the instability criterion based on the principle of irreversible thermodynamics can be used to determine the instability region of material flow in the large plastic deformation. Additionally, the hot processing map can be used to explain various plastic deformation mechanisms,

determine the rheological instability zone which should be avoided in the hot working process, and finally determine the temperature and strain rate ranges to obtain excellent microstructure. Based on the abovementioned analysis, it can be concluded that the optimal thermodynamic parameter range is related to the superplastic or dynamic recrystallization region in the energy dissipation diagram. In addition, other deformation mechanisms may have residual defects in the deformed component, eventually leading to substandard material properties. Thus, those deformation mechanisms should be avoided during the deformation process.

**2.4.1 Energy dissipation map**

Based on the dynamic material model theory, in a thermodynamic closed system of material plastic deformation, the relationship among the energy  $J$  involved in microstructure evolution, the energy  $G$  dissipated by plastic deformation ( $P=G+J$ ), and strain rate sensitivity index  $m$  can be expressed by Eq.(19), as follows:

$$m = \frac{dJ}{dG} = \frac{\dot{\epsilon}d\sigma}{\sigma d\dot{\epsilon}} = \frac{d(\ln \sigma)}{d(\ln \dot{\epsilon})} \tag{19}$$

According to the simulated thermal compression test results, the relationship curves of  $\ln\sigma - \ln\dot{\epsilon}$  under different temperature and strain conditions can be obtained, as shown in Fig.9.

Based on the  $\ln\sigma - \ln\dot{\epsilon}$  curves, the calculation method of Prasad energy dissipation map can be used to obtain the deformation energy dissipation map of IN706 superalloy. Usually, this method fits a cubic polynomial for a given deformation temperature, and then the strain velocity sensitivity index  $m$  can be calculated, as expressed by Eq.(20–22), as follows:

$$\ln \sigma = a + b \ln \dot{\epsilon} + c (\ln \dot{\epsilon})^2 + d (\ln \dot{\epsilon})^3 \tag{20}$$

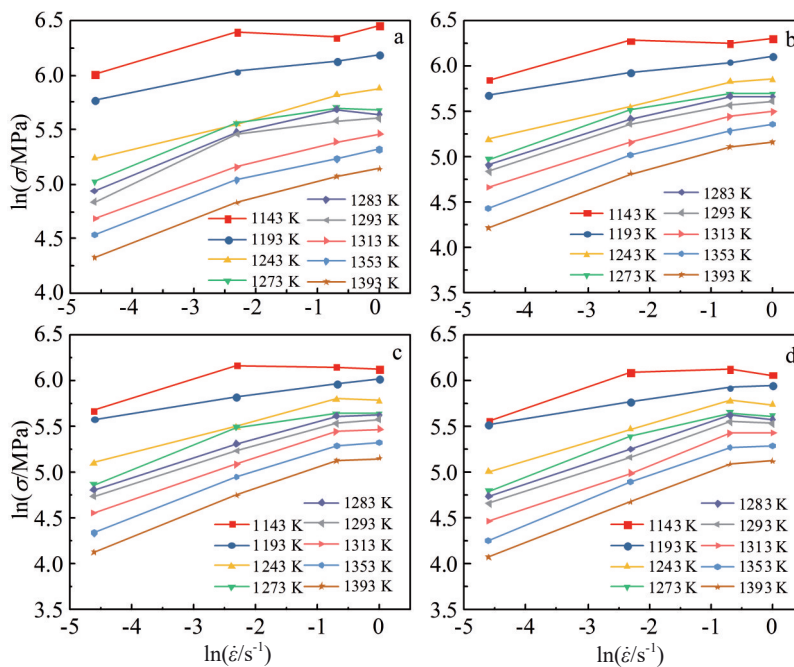


Fig.9 Relationships of  $\ln\sigma - \ln\dot{\epsilon}$  under different temperatures and strains: (a)  $\epsilon=0.2$ , (b)  $\epsilon=0.4$ , (c)  $\epsilon=0.6$ , and (d)  $\epsilon=0.8$

$$m = \frac{d(\ln \sigma)}{d(\ln \dot{\epsilon})} = b + 2c \ln \dot{\epsilon} + 3d (\ln \dot{\epsilon})^2 \quad (21)$$

$$\eta = \frac{2m}{m + 1} \quad (22)$$

where  $a$ ,  $b$ ,  $c$ , and  $d$  are the fitting coefficients;  $\eta$  is the energy dissipation rate. After the strain rate sensitivity index  $m$  is obtained, the energy dissipation rate  $\eta$  under different

deformation temperatures and strain rates can be calculated by Eq. (22). Then, the energy dissipation map under specific strains are obtained using the interpolation method, and the results are shown in Fig.10 and Fig.11.

According to Fig.11, there are two regions with high energy dissipation rates. One is the upper left region with strain rate of  $0.01 \text{ s}^{-1}$  and temperature around 1393 K. The other is the

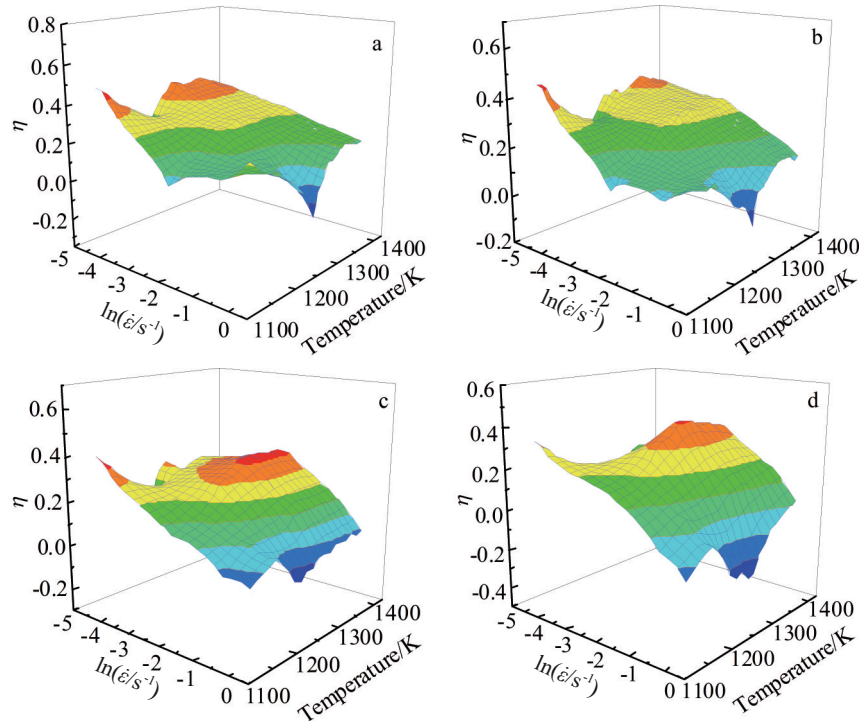


Fig.10 3D energy dissipation maps of IN706 superalloy at different strains: (a)  $\epsilon=0.2$ , (b)  $\epsilon=0.4$ , (c)  $\epsilon=0.6$ , and (d)  $\epsilon=0.8$

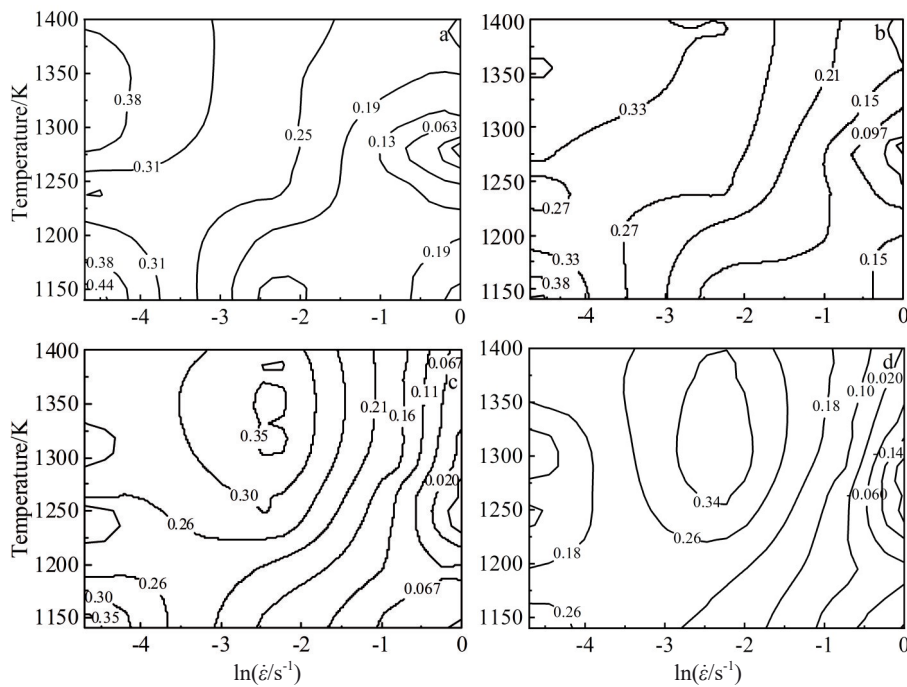


Fig.11 Energy dissipation contour maps of IN706 superalloy at different strains: (a)  $\epsilon=0.2$ , (b)  $\epsilon=0.4$ , (c)  $\epsilon=0.6$ , and (d)  $\epsilon=0.8$

lower left corner region with strain rate of  $0.01 \text{ s}^{-1}$  and temperature around 1143 K. The lower the strain rate, the greater the dissipation rate. In the region with strain rate of  $1 \text{ s}^{-1}$  and temperature of 1273–1283 K, the dissipation rate is the smallest. Comparing the energy dissipation rates under characteristic strain conditions, it can be found that the distributions of energy dissipation rates under each strain condition are similar, but when the strain rate is lower than  $0.01 \text{ s}^{-1}$ , the level of dissipation rate is gradually decreased with the increase in strain. When the strain rate is  $0.1 \text{ s}^{-1}$ , the dissipation rate is gradually increased with the increase in the reduction deformation amount, which indicates that with the strain rate of  $0.1 \text{ s}^{-1}$ , the proportion of the energy involved in the microstructure evolution is increased with the increase in the plastic deformation amount.

The region with low energy dissipation rate appears in the region with temperature of 1273–1283 K and high strain rate, indicating that the energy dissipation in this region is mainly used for deformation at high temperature. The energy involved in the microstructure evolution is relatively small, so it is easy to induce the deformation mechanism of defects. The peak value of energy dissipation rate in Fig.11 is located in the low strain rate region, indicating that the corresponding process parameters in this region should be the optimal process parameters for the hot working process of IN706 superalloy.

#### 2.4.2 Murty instability criterion

Considering that the strain rate sensitivity index  $m$  is not constant, Murty et al.<sup>[29-30]</sup> proposed a rheological instability criterion, which is applicable to any stress-strain curve. In this criterion, the dissipative covariate  $J$  is related to the

organizational evolution, which can be expressed by the integral equation  $J=P-G$ . Since  $P=\sigma\dot{\epsilon}$ , when  $m=1$ , the maximum value of  $J$  ( $J_{\max}$ ) can be expressed by Eq.(23), as follows:

$$J_{\max} = \frac{P}{2} = \frac{\sigma\dot{\epsilon}}{2} \quad (23)$$

Then, the dissipation efficiency factor  $\eta$  can be defined, as follows:

$$\eta = \frac{J}{J_{\max}} = \frac{P-G}{P/2} = 2\left(1 - \frac{G}{P}\right) = 2\left(1 - \frac{1}{\sigma\dot{\epsilon}} \int_0^{\dot{\epsilon}} \sigma d\dot{\epsilon}\right) \quad (24)$$

Therefore, the plastic instability criterion is shown in Eq.(25), as follows:

$$\xi = \frac{2m}{\eta} - 1 < 0 \quad (25)$$

The Murty instability criterion is based on the continuous theory of large plastic deformation. Since it is not an empirical formula, it can be applied to any type of flow stress and strain rate curves. At the same time, Murty instability criterion is the most promising method because of its simple form, convenient calculation, and rigorous analysis. Based on the experimental results in this research and Murty instability criterion, 3D instability maps under different conditions are obtained, as shown in Fig.12.

#### 2.4.3 Hot processing map establishment

Based on the energy dissipation maps in Fig.11 and Murty instability maps in Fig.12, the hot processing maps under the characteristic strains are shown in Fig.13. The colored regions indicate the unstable regions determined by Murty instability criterion.

It can be found that when the strain is 0.2, the instability region in Fig.13a is located in the region with deformation temperature of 1273 K and strain rate of  $1 \text{ s}^{-1}$ . When the strain

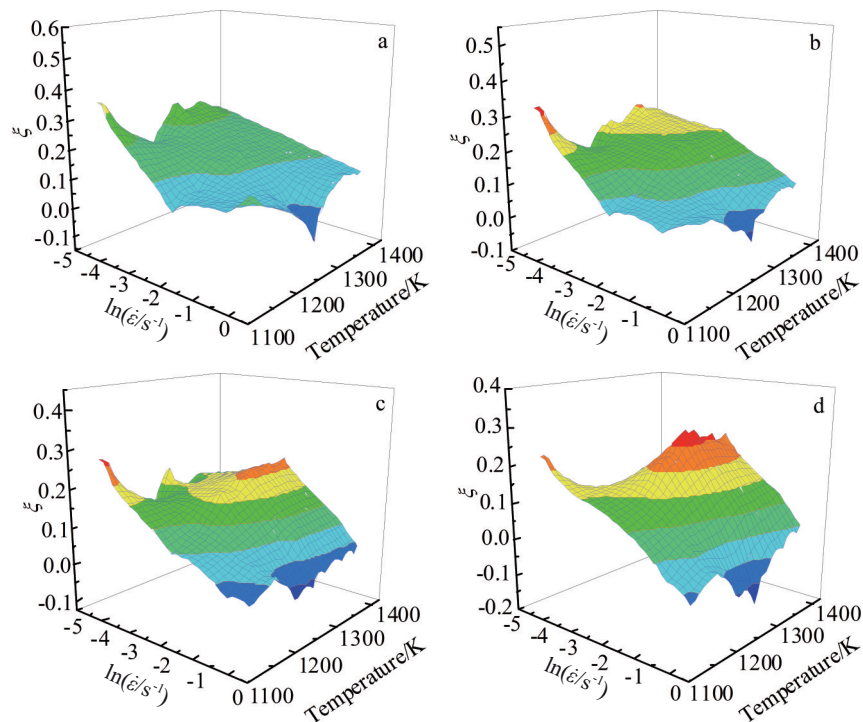


Fig.12 3D instability maps based on Murty instability criterion at different strains: (a)  $\epsilon=0.2$ , (b)  $\epsilon=0.4$ , (c)  $\epsilon=0.6$ , and (d)  $\epsilon=0.8$

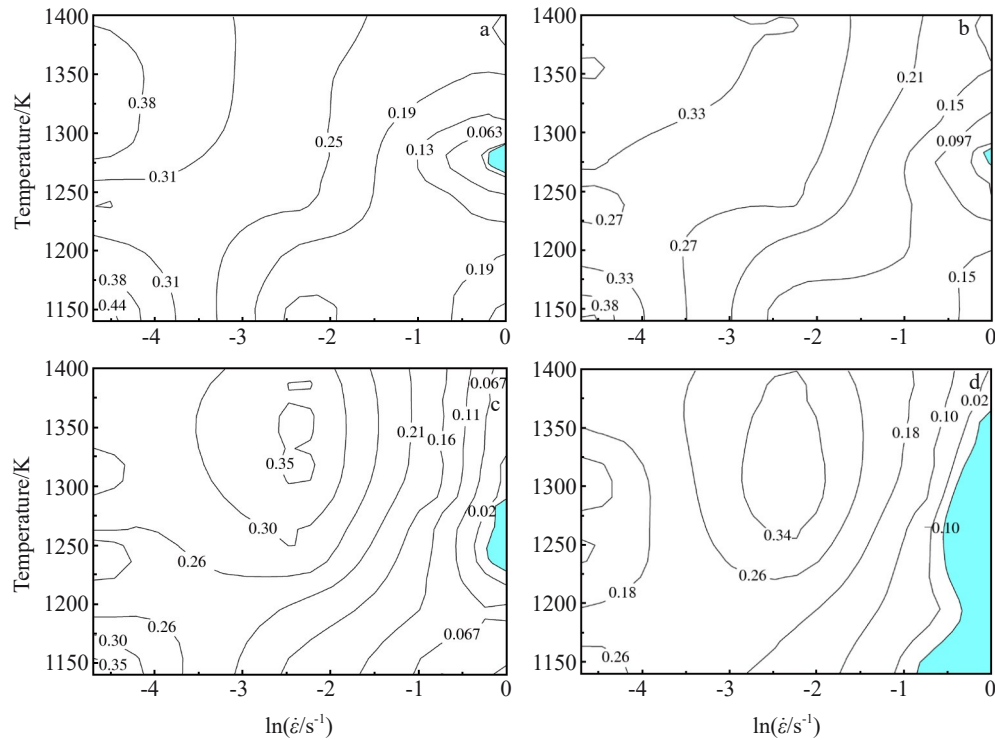


Fig.13 Hot processing maps based on Murty instability criterion at different strains: (a)  $\varepsilon=0.2$ , (b)  $\varepsilon=0.4$ , (c)  $\varepsilon=0.6$ , and (d)  $\varepsilon=0.8$

is 0.4, the location of unstable region is basically unchanged, but the area shrinks slightly, as shown in Fig.13b. When the strain is 0.6, the unstable region slightly changes: the area is larger, the temperature range is 1225–1273 K, and the strain rate range slightly expands. When the strain is 0.8, the instability region further expands, and the temperature range is 1143–1353 K, and the strain rate is  $0.5\text{--}1\text{ s}^{-1}$ . These results indicate that when the strain becomes larger, the strain rate also becomes larger.

Generally, the largest area of energy dissipation in the hot working diagram is the optimal hot working area, and the corresponding area is related to the energy involved in microstructure evolution of higher proportion during the thermal deformation process, which is conducive to the deformation mechanism, such as dynamic recrystallization, for the optimization of microstructure and properties. Therefore, based on the instability region and 3D energy dissipation rate diagram of the hot processing maps, the optimal processing window in this research should be strain rate of  $0.1\text{ s}^{-1}$  and temperature of 1313–1353 K.

### 3 Conclusions

1) IN706 superalloy exhibits the typical flow behavior. The stress is sensitive to the deformation temperature and strain rate.

2) The constitutive equation based on Arrhenius model with strain compensation shows good prediction accuracy with  $R=0.9846$  and  $AARE=6.5922\%$ .

3) The energy dissipation maps of IN706 superalloy is obtained based on the dynamic material model, and the hot processing map is established based on Murty criterion. The

optimal processing window should be strain rate of  $0.1\text{ s}^{-1}$  and temperature of 1313–1353 K.

### References

- 1 Mukherji D, Gilles R, Barbier B et al. *Scripta Materialia*[J], 2003, 48(4): 333
- 2 Tian Wei, Zhang Shaoping, Zhong Yan et al. *Rare Metal Materials and Engineering*[J], 2024, 53(6): 1726 (in Chinese)
- 3 Kuhlman G W, Chakrabarti A K, Beaumont R A et al. *Superalloys*[J], 1994, 718(625): 441
- 4 Mannan S, Patel S, Debarbadillo J. *Ninth International Symposium on Superalloys*[C]. Warrendale: TMS, 2000: 449
- 5 Sharma P, Chakradhar D, Narendranath S. *Journal of Manufacturing Processes*[J], 2016, 24: 170
- 6 Maharaj C, Morris A, Dear J P. *Materials Science and Engineering A*[J], 2012, 558: 412
- 7 Han J W, Jung S H, Lee H W. *Metals and Materials International*[J], 2022, 28: 733
- 8 Kindrachuk V, Wanderka N, Banhart J. *Materials Science and Engineering A*[J], 2006, 417: 82
- 9 Yenusah C O, Ji Y, Liu Y et al. *Computational Materials Science*[J], 2021, 187: 110123
- 10 Ding J, Xue S, Shang Z et al. *Materials Science and Engineering A*[J], 2021, 804: 140718
- 11 Zhang W B, Yang H J, Liu C R et al. *Rare Metal Materials and Engineering*[J], 2024, 53(6): 1592
- 12 Theska F, Stanojevic A, Oberwinkler B et al. *Materials Science and Engineering A*[J], 2020, 776: 138967

- 13 Zhao S, Xie X, Smith G D et al. *Materials Science and Engineering A*[J], 2003, 355(1-2): 96
- 14 Mukherji D, Strunz P, Genovese D D et al. *Metallurgical and Materials Transactions A*[J], 2003, 34: 2781
- 15 Ducki K J. *Archives of Metallurgy and Materials*[J], 2011, 47(1): 33
- 16 Kim H, Oh H, Bae H J et al. *Journal of Materials Research and Technology*[J], 2022, 21: 2145
- 17 Marsh C, Kaoumi D. *Materials Science and Engineering A*[J], 2017, 707: 136
- 18 Kim C, Park J, Hong H U et al. *Journal of Alloys and Compounds*[J], 2022, 900: 163479
- 19 Wanderka N, Naundorf V, Banhart J et al. *Surface and Interface Analysis*[J], 2004, 36(5-6): 546
- 20 Shibata T, Shudo Y, Takahashi T et al. *Superalloys*[M]. New York: TMS, 1996: 627
- 21 Ashtiani H R R, Shahsavari P. *Mechanics of Materials*[J], 2016, 100: 209
- 22 Zeng Z P, Jonsson S, Zhang Y S. *Materials Science and Engineering A*[J], 2009, 505: 116
- 23 Cai J, Li F G, Liu T Y et al. *Materials & Design*[J], 2011, 32(3): 1144
- 24 Ren F C, Chen J. *Journal of Iron and Steel Research*[J], 2013, 20: 118
- 25 Zhang J, Di H, Wang X et al. *Materials & Design*[J], 2013, 44: 354
- 26 Zhang J, Di H, Mao K et al. *Materials Science and Engineering A*[J], 2013, 587: 110
- 27 Wolla D W, Davidson M J, Khanra A K. *Materials & Design*[J], 2015, 65: 83
- 28 Li J, Li F G, Cai J et al. *Materials & Design*[J], 2012, 42: 369
- 29 Murty S V S N, Rao B N. *Materials Science and Engineering A*[J], 1998, 254(1-2): 76
- 30 Murty S V S N, Rao B N. *Journal of Physics D: Applied Physics*[J], 1998, 31(22): 3306

## IN706 高温合金的高温压缩变形力学行为及本构方程

杜立成, 高峰, 董卓林

(中国航发航空科技股份有限公司, 四川 成都 610503)

**摘要:** IN706 高温合金对热加工工艺参数特别敏感, 在 1143~1393 K、应变速率为 0.01、0.1、0.5 和  $1 \text{ s}^{-1}$  的等温压缩条件下将 IN706 高温合金分别压缩 30%、45% 和 60%, 研究了 IN706 高温合金的流变应力。采用指数型 Zener-Hollomon 方程来描述应变和温度对热变形的影响, 同时在考虑应变补偿的本构方程中考虑了  $\alpha$ 、 $n$ 、 $Q$  和  $\ln A$  等不同材料常数的应变效应, 并对相关系数  $R$  和平均绝对相对误差进行了验证。在构建本构方程的基础上, 绘制了 IN706 高温合金的热加工图, 并根据 Murty 准则给出了不稳定区域。结果表明, 应变速率  $0.1 \text{ s}^{-1}$ 、温度 1313~1353 K 是合理的热加工工艺参数窗口。

**关键词:** IN706 高温合金; 力学行为; 本构方程; 热加工图; 应变效应

作者简介: 杜立成, 男, 1983 年生, 博士, 中国航发航空科技股份有限公司, 四川 成都 610503, E-mail: 115418225@qq.com